Understanding the role of VSC control strategies in the limits of power electronics integration in AC grids using modal analysis

Rayane Mourouvin, Juan Carlos Gonzalez-Torres, Jing Dai, Abdelkrim Benchaib, Didier Georges, Seddik Bacha

Version of Record: https://www.sciencedirect.com/science/article/pii/S0378779620307288
Manuscript_089883b748af4bcef80c64eecfb353ed

Understanding the Role of VSC Control Strategies in the Limits of Power Electronics Integration in AC Grids using Modal Analysis

Rayane Mourouvin[1,2,**], Juan Carlos Gonzalez-Torres[1], Jing Dai[1,3], Abdelkrim Benchaib[1], Didier Georges[1,2], Seddik Bacha[1,4]

Abstract

In this article, the interactions between AC grid and existing VSC control modes are analyzed. First, three VSC control modes, namely grid-feeding, grid-supporting and grid-forming, are compared with each other in order to assess VSC/grid coupling level. Then, in order to underscore the growing role of VSCs in transmission systems, an elementary benchmark network is considered. It includes an equivalent SM (Synchronous Machine), a VSC, a load and a transmission line with a varying electrical distance. Thereafter, a modal analysis is conducted on this model to study the interactions between the different VSC controls and the SM dynamics using a Matlab/Simulink environment. The converter penetration rate is represented by a variable power ratio between the converter and the machine, while the electrical distance by an RL dynamic impedance. This approach makes it possible to assess the stability limits on the VSC share imposed by the system strength. Negative interactions are identified and recommendations for novel converter control strategies proposed. Besides, the influence of the AVR with the VSC in grid-forming as well as PLL-related stability issues with the VSC in grid-feeding or grid-supporting are shown to be the key limiting factors for increasing the penetration of PE-based sources.

Keywords: renewable energy, Voltage Source Converter, synchronous machines, power electronics, grid-forming, grid-supporting, grid-feeding, PLL, small-signal stability.

1. Introduction

Due to climate change, international policy-makers have to work on agreements to drastically reduce the emission of greenhouse gases in the upcoming decades. This constitutes a major concern for the energy sector and, in consequence, more and more renewable energy sources (RES) are connected to the power systems, mainly through Power Electronic (PE) converters. Historically, the only function of RES was to produce as much energy as possible, except the hydro power plants which are dispatchable. However, since their power contributions within the grid is reaching an unprecedented level, Transmission System Operators (TSO) expect that the converters also provide ancillary services that used to be realized by the Synchronous Machines (SM) of traditional thermal and hydro power plants. By 2050, renewable energy is expected to produce 70-85% of electricity in an attempt to limit global warming to 1.5°C [1]. In consequence, the available hydro power plants, which covered 14.4% of the annual power consumption in France in 2018 [2], would be highly solicited. Even if 100% PE-based grid scenarii are unlikely to occur, hybrid systems with

*Institute of Engineering Univ. Grenoble Alpes
**Corresponding author. Email: rayane.mourouvin@supergrid-institute.com
[1]Supergrid Institute SAS, 23 rue de Cyprian, 69100 Villeurbanne, France
[2]Univ. Grenoble Alpes, CNRS, Grenoble INP*, GIPSA-lab, 38000 Grenoble, France
[3]Université Paris-Saclay, CentraleSupélec, CNRS, Laboratoire de Génie Electrique et Electronique de Paris, 91192, Gif-sur-Yvette, France. Sorbonne Université, CNRS, Laboratoire de Génie Electrique et Electronique de Paris, 75252, Paris, France
[4]Univ. Grenoble Alpes, CNRS, Grenoble INP*, G2Elab, 38000 Grenoble, France

a high penetration of PE and the remaining SM including hydro power plants and synchronous condensers could be the future tendency. For such systems, it is essential to study the interactions between large PE-based stations and SMs.

In the literature, some studies have been published to tackle the interactions between the Voltage Source Converters (VSC) in grid-feeding mode and SM and show penetration limit through modal analysis, with different notions of power ratio [3, 4, 5, 6]. The notion of power penetration ratio has also been introduced in experimental setups recently [7]. The impacts of critical dynamics such as the Phase-Locked-Loop (PLL) and transmission lines (characterized by the Short-Circuit Ratio, or SCR) have been highlighted for grid-feeding VSCs [8]. The impact of the transmission lines was also pointed out recently for grid-supporting strategies using droop controllers [9].

Following the development of grid-forming control strategies for transmission systems [10, 11], the grid-forming control has become an accepted solution for weak grids, i.e. high-impedance grids and low-inertia systems [12]. The impact of the converter's electrical distance to the main grid [13] and its interactions with existing machines when controlled as a voltage source [14] or operating in grid-forming mode [15] have been recently studied using the notion of power ratio. Among different grid-forming strategies, droop [13] and Virtual Synchronous Machine (VSM)[16] controls are now the most commonly used in literature [17]. In addition, a comparison of existing grid-forming control strategies such as dispatchable virtual oscillator (dVOC) [18] and matching synchronous machines [19] was conducted using time-domain simulations of multiple-bus systems [20]. To the authors' best knowledge, there are no studies that compare current-source modes and voltage-source modes of VSC at the same operating conditions for assessing the stability limits of the system. The novelty of the paper is to provide a comparative analysis between the current-source mode and voltage-source mode at the same grid conditions and power setpoints. By acting on the critical dynamics of the system and using modal analysis tools, the results suggest negative interactions between the SM's AVR and the grid-forming control of the VSC, which have not been highlighted in the literature so far. Last but not least, different scenarii are studied by simulations with a multi-machine system in order to deepen the modal analysis results.

The paper is organized as follows: in Section 2, the test system and its nonlinear differential equations are presented. In Section 3, the modal analysis method and results are presented, which are validated using a Matlab/Simulink state-space model and a multi-machine system developed in Modelica language in different scenarii in Section 4. Finally, the conclusions and future work are discussed in Section 5.

2. System Modeling

2.1. Description of the test system

For the study, an elementary benchmark is considered, which is composed of one VSC with its LC filter, one synchronous machine, the two connected by an AC line, and a load at the point of common coupling (PCC) located on the VSC side, as given in Fig. 1.

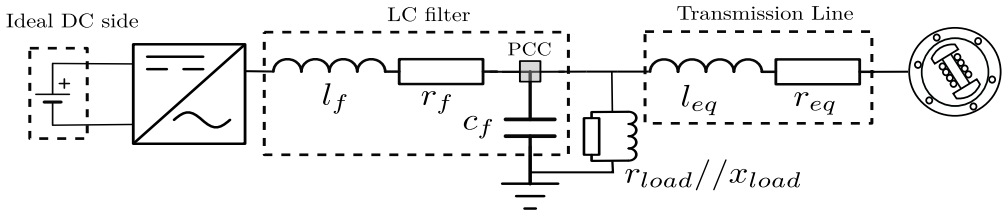

Fig. 1. Considered benchmark for the study.

In order to assess the system stability, the system is linearized around an operating point. A modal analysis is performed for different PE penetration levels and AC grid strengths, i.e. for different values of

the line impedance. The penetration of PE is modeled by the *Power Ratio*, denoted by P_R and defined as:

$$P_R = \frac{S_{vsc}}{S_{sm} + S_{vsc}} = \frac{S_{vsc}}{S_{base}} \tag{1}$$

where S_{vsc} and S_{sm} are respectively the VSC and SM rated powers and S_{base} is the system base power.

2.2. Synchronous machine model and control

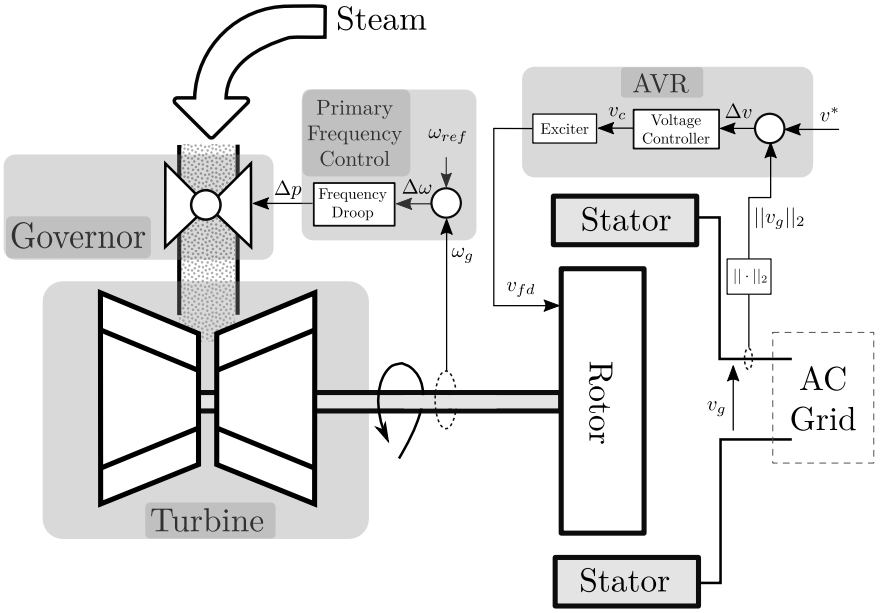

Fig. 2. Synchronous Machine (SM) with its voltage and frequency controls.

As the SM are currently the most commonly used for power generation, their dynamics need to be taken into account to highlight possible negative interactions [4], [5]. These interactions could not be tackled with the grid modeled as an equivalent voltage source [13] or with only electromechanical models [9]. Indeed, SM have several controllers among which the voltage regulator, or AVR, can have a negative impact on the system. A conceptual scheme of the SM control model is given in Fig. 2. The SM model considered in this study is a reduced-order 1-axis model of a steam-powered SM that captures both electromechanical and electromagnetic dynamics. This model was developed in details in [21] and the considered equations are given in Appendix 1.

2.3. Converter modeling & control

This section describes the converter model and their control schemes, which can be classified into two categories [22] and are adapted here for transmission grids:

- **Current source control**: the VSC follows power references and injects a current in phase with the network thanks to the PLL synchronizing unit. It corresponds to the *grid-feeding*, also called *grid-following* mode. In the *grid-supporting* mode, the power references are adjusted to provide grid services;
- **Voltage source control**: the VSC works as a voltage source and is thus able to operate in islanded mode. It uses the power variations to synchronize with the grid so that no PLL is needed anymore. It corresponds to the *grid-forming* mode.

Both classes use cascaded loops including a current control loop with potential current limiting actions to protect the semiconductor devices. Indeed, the overcurrent capability of VSCs is only 110%, which is much smaller than traditional SMs [23]. Nevertheless, the impact of current limiting control on stability is not considered in this study. In both classes, the inner loop control uses PI controllers whose gains are tuned using pole placement methods [24], [25].

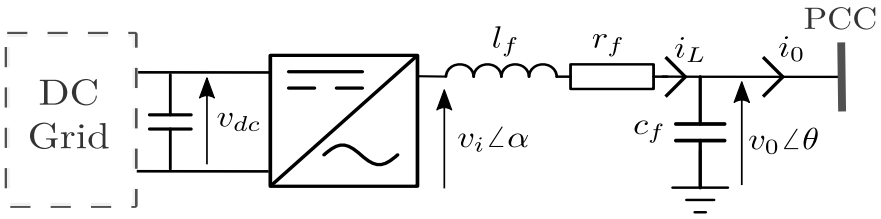

Fig. 3. Equivalent electrical scheme of VSC with LC filter.

The VSC is considered with an LC filter, as described in Fig. 3. In the current source mode, the control scheme regulates the line current i_L by acting on the output voltage v_i. To synchronize with the grid voltage v_0, the scheme needs a PLL to capture the grid-frequency and the PCC electrical angle.

2.3.1. Physical model of VSC

The VSC model considered here is an ideal voltage source where the dynamics of the switches are neglected. In addition, the PWM control dynamics are neglected and thus the actual output voltage is considered to be equal to the reference voltage given by the control law:

$$v_i^{dq} = v_{i,ref}^{dq} \tag{2}$$

2.3.2. Outer loop for current-source control

In this paper, current source control refers to the scheme that uses the VSC voltage output as the control variable to regulate the branch current passing through the LC filter. The general scheme of this type of control is given in Fig. 4 and covers grid-feeding [3, 8, 4] and grid-supporting [9] strategies.

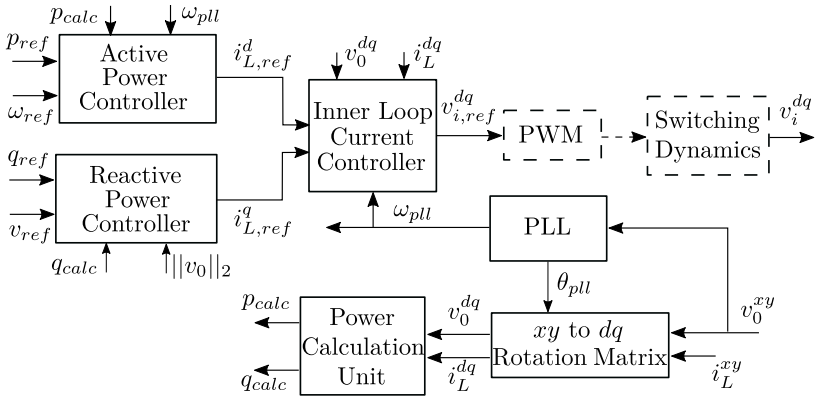

Fig. 4. VSC control in current source mode: grid-feeding and grid-supporting.

With the grid-feeding control, the outer power loops use pure integral controllers, with k_{ip} as the control gain, to regulate the filtered active and reactive powers to their references. In grid-supporting, an additional

droop is added to change the active and reactive power references to contribute respectively to frequency and voltage stability, which are given by:

$$p'_{ref} = p_{ref} + K_{p\omega} \cdot (\omega_{ref} - \omega_{pll}) \tag{3}$$

$$q'_{ref} = q_{ref} + K_{qv} \cdot (v_{ref} - ||v_0^{dq}||_2) \tag{4}$$

where p_{ref}, q_{ref}, ω_{ref} and v_{ref} are respectively the references of active power, reactive power, frequency and voltage in per-unit obtained from the load flow solution. The droop gains $K_{p\omega}$ and K_{qv} are used to provide support to the grid, hence the name grid-supporting. In grid feeding mode, $K_{p\omega} = K_{qv} = 0$.

The power control loop which generates the current reference in dq-frame for the inner current controller is:

$$i_{L,ref}^{dq} = k_{ip} \cdot [\epsilon_p, \epsilon_q]^T \tag{5}$$

where $\dot{\epsilon}_p = p'_{ref} - p_{avg}$ and $\dot{\epsilon}_q = q'_{ref} - q_{avg}$ are respectively the active and reactive power control errors. The filtered measured powers are calculated as:

$$\begin{bmatrix} \dot{p}_{avg} \\ \dot{q}_{avg} \end{bmatrix} = \omega_{c,power} \cdot \begin{bmatrix} p_{calc} - p_{avg} \\ q_{calc} - q_{avg} \end{bmatrix} \tag{6}$$

where $p_{calc} = v_0^d \cdot i_L^d + v_0^q \cdot i_L^q$ and $q_{calc} = v_0^q \cdot i_L^d - v_0^d \cdot i_L^q$ are the calculated output powers for the current-source mode. Finally, the PLL is modeled by a PI controller with a low-pass filter, as described in [3, 26]:

$$\dot{\hat{v}}_0^{dq,pll} = \omega_{c,pll} \cdot (v_0^{dq,pll} - \hat{v}_0^{dq,pll}) \tag{7}$$

$$\omega_{pll} = k_{i,pll} \cdot \epsilon_{pll} + k_{p,pll} \cdot \dot{\epsilon}_{pll} \tag{8}$$

$$\dot{\theta}_{pll} = \omega_{base} \cdot \omega_{pll} \tag{9}$$

with $k_{i,pll}$ and $k_{p,pll}$ as the PI gains of the controller and $\dot{\epsilon}_{pll} = 0 - \hat{v}_0^{dq,pll}$, $\hat{v}_0$ the filtered signal of v_0 and $\omega_{c,pll}$ the low-pass filter cutoff frequency.

2.3.3. Outer loop for voltage-source control

In voltage-source mode, the control scheme regulates the PCC voltage v_0, which is no longer an external disturbance from the control point of view. The scheme relies on cascaded loops, described in Fig. 5, where it uses the branch current i_L to act on v_0 and uses the VSC output voltage v_i to control i_L. The synchronization with the grid is insured by the outer-loop control, i.e. grid-forming, thus no PLL is needed any more. This control scheme for grid-forming is the most commonly spread in literature even though it requires a good enough estimation of both the filter inductance and capacitance to control the PCC voltage and a physical LC filter at the VSC output. To address this issue, some other grid-forming control schemes have emerged recently to avoid the voltage control loop and act as current sources [27]. However, they remain out of the scope of this article.

The outer loop controls use the variations of active power and reactive power to respectively synchronize with the grid and maintain a certain voltage amplitude.

The active power control for the droop and the VSM schemes are, respectively:

$$\omega = \omega_{ref} + m_{p\omega} \cdot (p_{ref} - p_{avg}) \tag{10}$$

$$\dot{\omega} = \frac{1}{2 \cdot H_c} \cdot (p_{ref} - p_{calc} - D_c \cdot \omega) \tag{11}$$

Then, the corresponding angle is calculated as

$$\dot{\theta} = \omega_{base} \cdot \omega \tag{12}$$

The output powers of the VSC in voltage-source mode are $p_{calc} = v_0^d \cdot i_0^d + v_0^q \cdot i_0^q$ and $q_{calc} = v_0^q \cdot i_0^d - v_0^d \cdot i_0^q$.

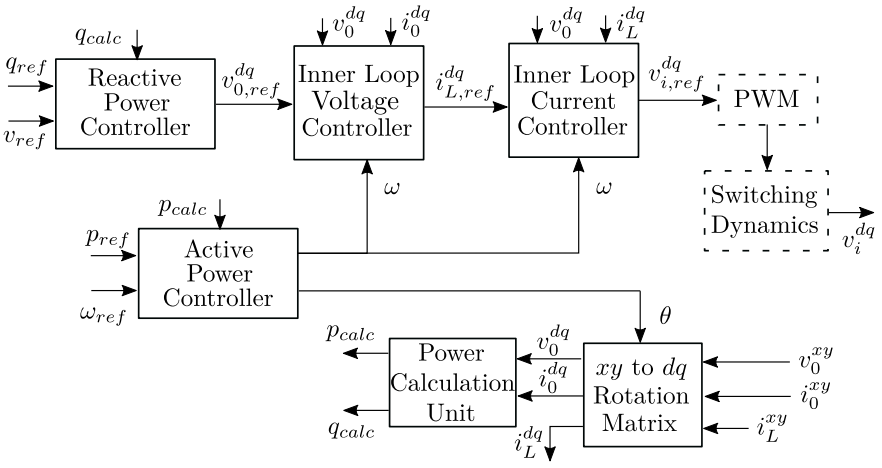

Fig. 5. VSC control in voltage source mode: grid-forming.

It is important to note that the gains of the VSM control are chosen to give the same steady-state response as grid-forming droop control [13].

The reactive power control is a droop controller and is similar to the implemented grid-forming droop and VSM controls, as in [13]. The option of using the state-space model of the SM [11, 27] is discarded in this study. The control law is:

$$e^* = v_{ref} + m_{qv} \cdot (q_{ref} - q_{avg}) \tag{13}$$

$$v_{0,ref}^{dq} = [e^*, 0]^T \tag{14}$$

2.3.4. Inner control loops

In grid-forming mode, as in Fig. 5, output terminal voltage and the line current are regulated using two cascaded loops. PI controllers are implemented for these loops and are tuned with pole placement method [24]. The voltage loop is designed to be ten times slower than the current loop to avoid potential interference [25]. The inner voltage control law is:

$$i_{L,ref}^{dq} = k_{iv} \cdot \epsilon_v^{dq} + k_{pv} \cdot \dot{\epsilon}_v^{dq} + \omega c_f \cdot \begin{bmatrix} 0 & -1 \\ 1 & 0 \end{bmatrix} \cdot v_0^{dq} + \alpha_i \cdot i_0^{dq} \tag{15}$$

with $\dot{\epsilon}_v^{dq} = v_{0,ref}^{dq} - v_0^{dq}$. The current reference generated from the voltage controller is then used in the current control law as:

$$v_{i,ref}^{dq} = k_{ii} \cdot \epsilon_i^{dq} + k_{pi} \cdot \dot{\epsilon}_i^{dq} + \omega l_f \cdot \begin{bmatrix} 0 & -1 \\ 1 & 0 \end{bmatrix} \cdot i_l^{dq} + \alpha_v \cdot v_0^{dq} \tag{16}$$

with $\dot{\epsilon}_i^{dq} = i_{L,ref}^{dq} - i_L^{dq}$. The output signal of the current control loop, $v_{i,ref}^{dq}$, refers to the desired voltage in dq-frame to be generated by the VSC internal actuators, which are not considered here.

The same current controller is used in all the grid-feeding, grid-supporting and grid-forming schemes. The inner current controllers based on PR (Proportional Resonant) control to regulate the VSC current in the stationary frame ($\alpha\beta$) [22, 28] are gaining more interest compared to the classical PI control [29, 30]. However, it remains out of this paper scope where the most prevalent VSC control schemes are considered to assess the stability limits.

2.4. Network modeling & interfaces

2.4.1. Interconnecting line model

The network is modeled as a dynamic RL line which connects the SM bus with voltage v_g to the load and VSC output filter bus with voltage v_0, as described by:

$$\frac{di_{eq}^d}{dt} = \frac{\omega_{base}}{l_{eq}} \cdot (v_g^d - v_0^d - r_{eq} \cdot i_L^d + \omega_g \cdot l_{eq} \cdot i_{eq}^q) \tag{17}$$

$$\frac{di_{eq}^q}{dt} = \frac{\omega_{base}}{l_{eq}} \cdot (v_g^q - v_0^q - r_{eq} \cdot i_{eq}^q - \omega_g \cdot l_{eq} \cdot i_{eq}^d) \tag{18}$$

The line impedance is defined in per-unit, to take into account the changes of the SM power ratings when acting on the power ratio. Indeed, an electrical line of 100 km will not have the same influence when connected to a 100 MVA machine or a 1000 MVA one. Then, considering a constant ratio $X_{eq}/R_{eq} = 10$, which is common in power system studies, the equivalent resistance can be calculated.

2.4.2. Load model

The load is modeled as a static $R_{load}//X_{load}$ load connected at the PCC. The impedances are calculated using the expected load setpoints in S.I.:

$$R_{load} = \frac{U_{base}^2}{P_{load}} \;\; ; \;\; X_{load} = \frac{U_{base}^2}{Q_{load}} \tag{19}$$

2.4.3. Global system & interfaces

From its description, the whole system appears to be a combination of several subsystems with their own dq-frame. To associate the equations at the load bus, an interface is needed between:

- {SM + line} in the SM dq-frame, denoted by DQ;
- {VSC + LC filter} aligned with the load bus voltage dq-frame, denoted by dq.

This association can be achieved using rotation matrices between the two different frames as:

$$\begin{bmatrix} x^D \\ x^Q \end{bmatrix} = \begin{bmatrix} \sin(\delta - \theta) & -\cos(\delta - \theta) \\ \cos(\delta - \theta) & \sin(\delta - \theta) \end{bmatrix} \cdot \begin{bmatrix} x^d \\ x^q \end{bmatrix} \tag{20}$$

3. Modal Analysis

3.1. Parameters and operating points

For the modal analysis, the parameters and input data of the system are given in Table 2 in Appendix 2. The VSC reactive power reference q_{ref} and the SM active power reference P_m^* are not fixed but are adjusted in order to have $||v_0|| = v^*$ and $\omega_g = \omega_{ref}$. The tuning of the grid-forming outer loops (active and reactive power controllers) is based on [25, 31]. For the grid-feeding and grid-supporting schemes, the values of the power filter, PI power control and droop gains are based on [9]. The feedforward gains α_v and α_i from (15) and (16) are boolean and their values depend on the activation of the feedforward action for each controller. For the current-source controlled strategies, $\alpha_v = 1$ as there is no voltage control loop. For grid-forming strategies, we choose $\alpha_v = 1$ and $\alpha_i = 0$ because the voltage controller feedforward action proves to cause instability [25].

3.2. Method for modal analysis

The system model gathers the state variables of the different components and can be rewritten in general form as:

$$\dot{x} = f(x, u) \tag{21}$$

with $x = \left[x_{1,SM}, \ldots, x_{n,SM}, x_{1,VSC}, \ldots, x_{m,VSC}, i_{eq}^{d}, i_{eq}^{q}\right]^T$, the state variable vector of the system, n being the order of the SM subsystem with $x_{i,SM}$ as state variables and m the order of the VSC subsystem with $x_{i,VSC}$ as state variables. The vertical vector $u = \left[p_{ref}, q_{ref}, v_{ref}, P_m^*, v^*, \omega_{ref}\right]^T$ is the system input vector. Using this state-space model, we define the setpoints of all the state variables corresponding to the load flow solution and we linearize the system around the operating point $\{u_0, x_0\}$ as:

$$\Delta\dot{x} = A \cdot \Delta x + B \cdot \Delta u \tag{22}$$

$$A := \left.\frac{\partial f}{\partial x}\right|_{u_0, x_0} \in \mathbb{R}^{(n+m+2)\times(n+m+2)} \tag{23}$$

$$B := \left.\frac{\partial f}{\partial u}\right|_{u_0, x_0} \in \mathbb{R}^{(n+m+2)\times 6} \tag{24}$$

where A is the state matrix and corresponds to the structural properties of the system since it does not depend on the input/output signals. The matrix B is the input matrix. By extracting the eigenvalues of the A-matrix, we can analyze the stability of the system around the nominal point. The participation factors of some specific critical modes will also be used to enrich the results. The method for calculating the normalized participation factors is detailed in [32].

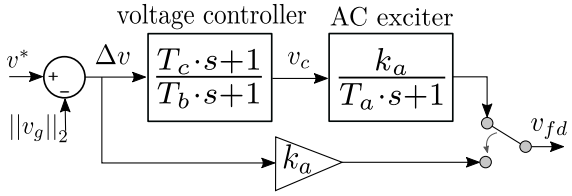

(a) Transfer function of the AVR and the switch when neglecting the AVR dynamics.

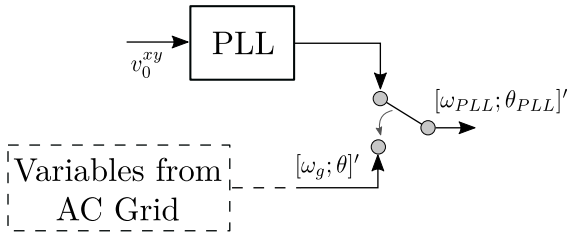

(b) Equivalent scheme of the PLL and the switch when neglecting the PLL dynamics.

Fig. 6. Illustrative scheme of the selection of AVR and PLL specific dynamics for studies.

In this paper, a study over some selected dynamics is also carried out to highlight harmful interactions between the SM and the VSC modes. The impact of the AVR dynamics (both lead-lag filter and AC exciter) on the system stability is studied. We compare the modal analysis results of two cases: the system with the AVR dynamics considered or neglected, as illustrated in Fig. 6a. For PLL-based controls, i.e. grid-feeding and grid-supporting, we compare two cases: one with the PLL dynamics, the other with an ideal PLL that captures the exact angle and exact frequency with no time-delay, as in Fig. 6b.

3.3. Results for PLL-based controls: grid-feeding and grid-supporting schemes

3.3.1. Influence of the power ratio

The results of the modal analyses for a given grid scenario with $x_{eq} = 0.33$ p.u. are displayed in Fig. 7 for the grid-feeding and grid-supporting cases. In these results we observe that the AVR has little impact on the system stability when the VSC is controlled in current-source mode. Indeed, the critical modes in Figs. 7a-7c and in Figs. 7b-7d are similar. On the other hand, the PLL appears to act as a limiting factor because the modes with an ideal PLL are all stable for $P_R \leq 0.8$ as described in Figs. 7f-7f. In addition, the grid-supporting control results in a higher penetration limit compared to grid-feeding.

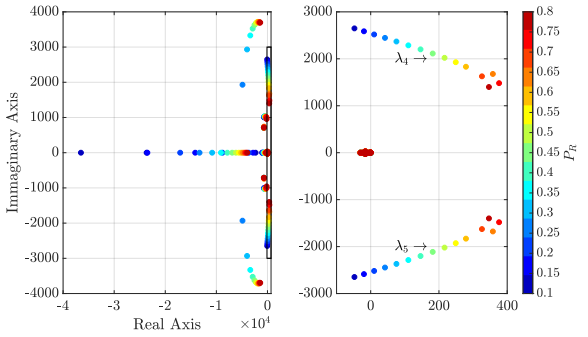

(a) Grid-feeding: nominal case

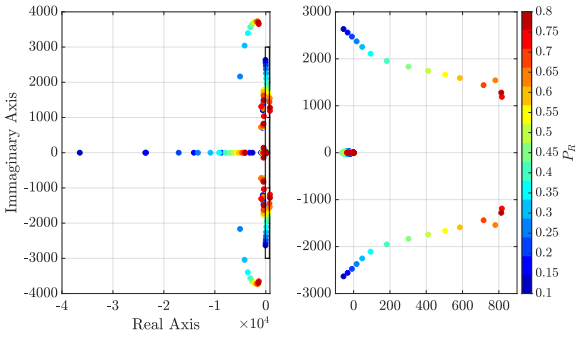

(b) Grid-supporting: nominal case

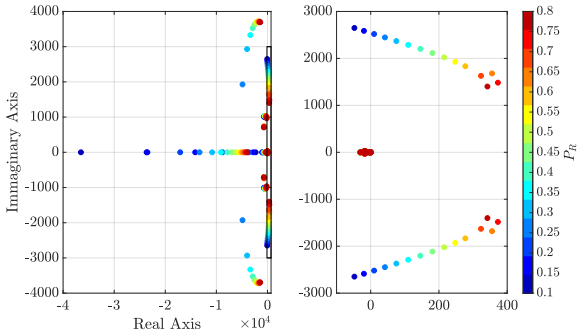

(c) Grid-feeding: no AVR dynamics

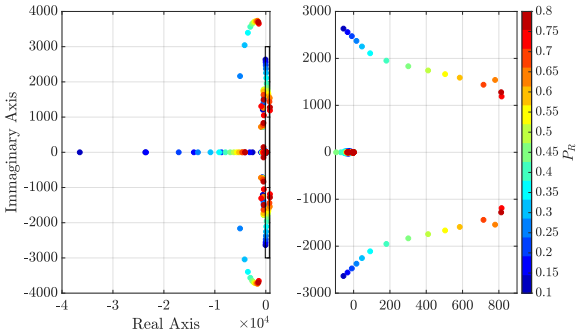

(d) Grid-supporting: no AVR dynamics

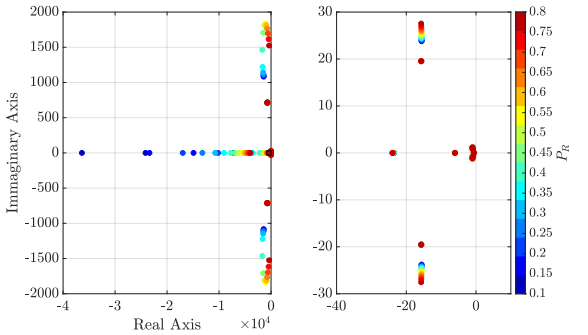

(e) Grid-feeding: "ideal" PLL

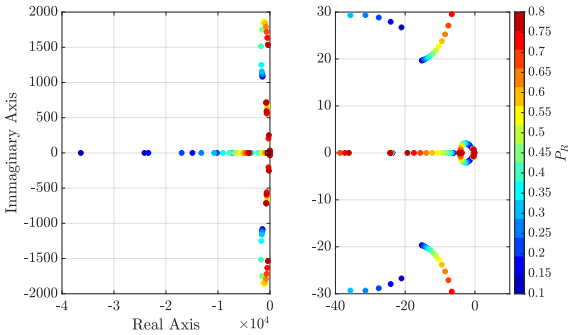

(f) Grid-supporting: "ideal" PLL

Fig. 7. Modal analysis results for different values of P_R with the VSC in grid-feeding (left-side) and grid-supporting (right-side) modes and $x_{eq} = 0.33$ p.u.

For further investigation, we calculate the participation factors of the critical mode, which is denoted by $\lambda_{4,5}$ in Fig. 7a, to show the potential destabilizing role of the PLL. The results are given in Fig. 8. It is clear that the PLL is responsible for the observed instability due to high participation factors when the power ratio is low. However, the larger the P_R, the smaller the PLL-variable participation. Indeed, as P_R increases, the share of the PLL is gradually replaced by the state variables of the passive components, namely the RL dynamics of the line and the LC filter, which implies that we can reach the structural limits of the current-source controlled VSCs regardless of the tuning of the PLL. This result confirms the limits of controlling VSCs in current sources when increasing their numbers in the AC grid, a phenomenon that cannot be observed when modeling the lines using static models [6]. The role of the PLL in destabilizing the system with PE-based sources attracts more and more attention from TSOs [33]. However, the nature of the oscillations appears to depend on the grid conditions and the PLL structure [34] and needs further investigation in the future.

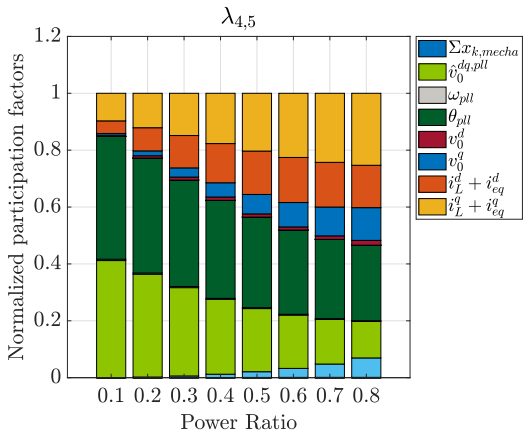

Fig. 8. Participation factors of the $\lambda_{4,5}$ mode for different values of the power ratio P_R whith the VSC in grid-feeding mode and $x_{eq} = 0.33$ p.u.

3.3.2. Influence of the electrical distance

In this paragraph, we perform a modal analysis on the PLL-based controlled VSCs for a given power ratio $P_R = 0.2$ and we change the line impedance. The results for the grid-feeding and grid-supporting are given in Fig. 9. As in the previous paragraph, it is clear that the AVR dynamics play no role on the small-signal stability of the system when the VSC is controlled either in grid-feeding or in grid-supporting. The system stability is still too sensitive to the power ratio and does not allow us to increase the penetration of PE above 30%. Nevertheless, the use of different grid-feeding control structures based on PR controllers could enhance the stability limits, since PR controllers exhibit better performances in weak grid conditions compared to PI controllers [35]. In the next section, we study the role that the grid-forming control can play in increasing those limits.

3.4. Results for PLL-free controls: grid-forming schemes

3.4.1. Influence of the power ratio

Since the grid-forming droop and VSM exhibit the same small-signal behavior [36], we only plot the results for the droop control with respect to the power ratio in Fig. 10. For the case $x_{eq} = 0.33$ p.u., we observe that the system is stable until around 45%, whereas it is stable for all the values of P_R when neglecting the AVR dynamics. To understand the critical mode evolution, we take a look at the critical modes $\lambda_{12,13}$ and $\lambda_{18,19}$ defined in Fig. 10a.

We calculate the participation factors of each mode for different values of P_R. The results, given in Fig. 11, show that both modes are low-frequency modes, since the participation factors of the SM mechanical

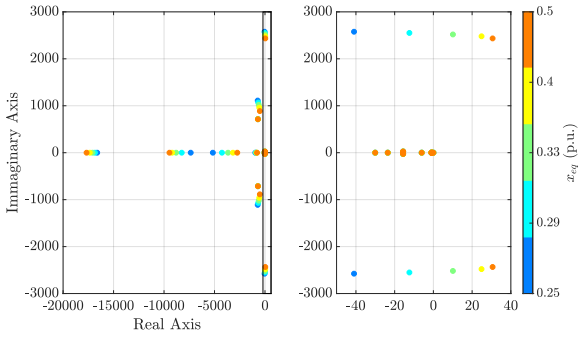

(a) Grid-feeding: nominal case

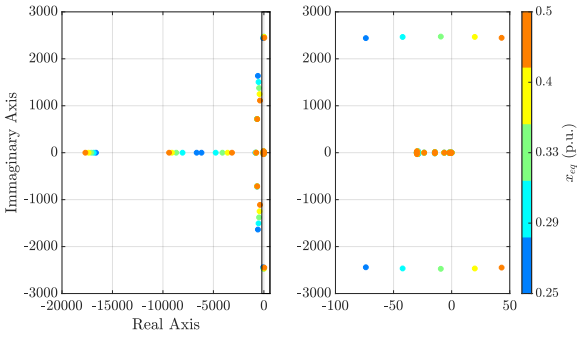

(b) Grid-supporting: nominal case

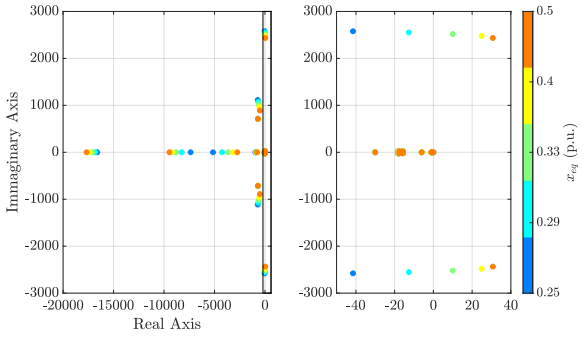

(c) Grid-feeding: no AVR dynamics

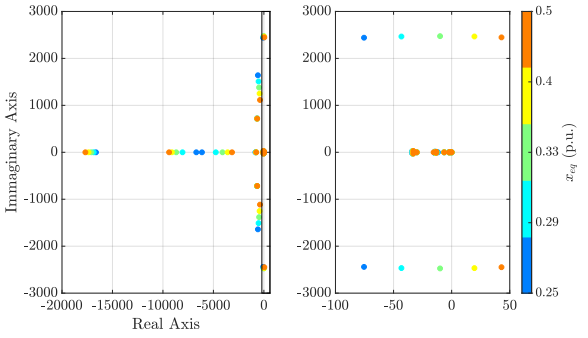

(d) Grid-supporting: no AVR dynamics

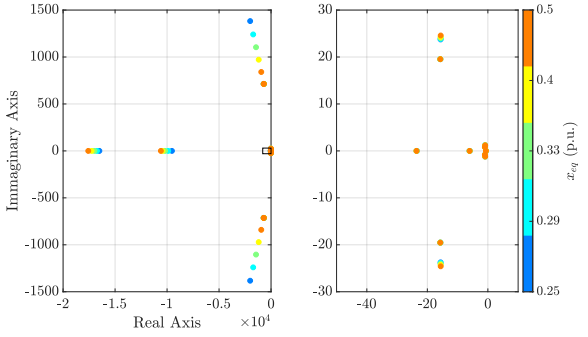

(e) Grid-feeding: "ideal" PLL

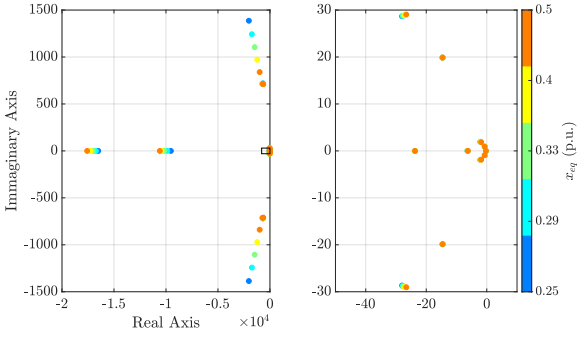

(f) Grid-supporting: "ideal" PLL

Fig. 9. Modal analysis results for different values of $x_{eq}$with the VSC in grid-feeding (left-side) and grid-supporting (right-side) modes and $P_R = 0.2$.

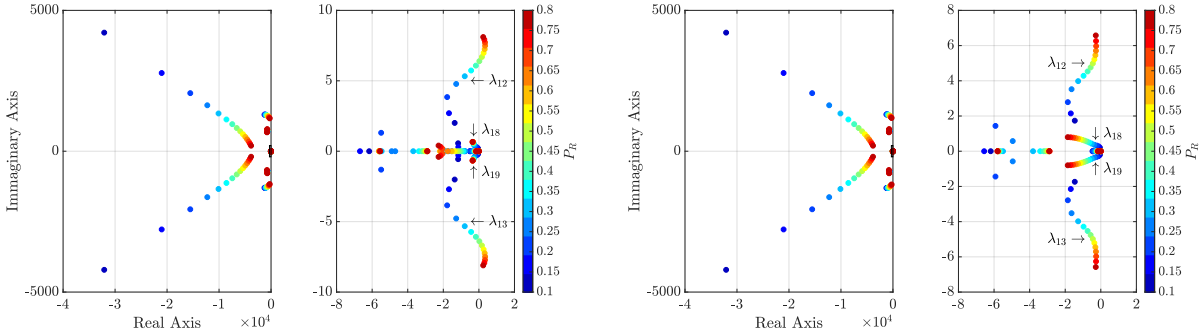

(a) Nominal state-space model

(b) State-space model with no AVR dynamics

Fig. 10. Modal analysis results for different values of P_R with the VSC in grid-forming (droop or VSM) mode and $x_{eq} = 0.33$ p.u.

variables, denoted by $x_{k,mecha}$, is important. Even if the role of the AVR dynamics is clear for modes $\lambda_{18,19}$, its impact on modes $\lambda_{12,13}$ is less evident using the participation factors. From Fig. 10, it is clear that the influence is weak but causes instability since the conjugate modes just slightly move beyond the imaginary axis, compared to the case where the AVR is neglected. In addition, compared to the electromagnetic dynamics, the time constants of the AVR lead-lag filter are rather slow, which fall in the range of electromechanical dynamics. It can explain why the undamped oscillatory modes $\lambda_{12,13}$ interact with the electromechanical variables. This result may seem counter-intuitive since 100% PE-based generation with VSCs in grid-forming has been proved to be stable [25]. In fact, the transition to 100% will go through a hybrid system where a high proportion of PE generators coexist with the remaining SMs. Because of their interactions, even with all converters working in grid-forming, this transition of the power systems should be more challenging than the 100% PE scenario [14].

3.4.2. Influence of the electrical distance

Here, we perform the modal analysis for a given grid scenario with $P_R = 0.45$ for different values of the line reactance x_{eq}. The results in Fig. 12 show the AVR dynamics move the modes to the right semi-plane. Even if the dependency of the modes on the electrical distance is small, bringing the SM closer to the VSC makes the system unstable. On the one hand, this result is counter-intuitive when compared to the PLL-controlled VSC. On the other hand, this result confirms the local interaction between the AVR and the synchronizing scheme of the grid-forming VSC.

Finally, for grid-forming controls (both droop and VSM), the interactions with AVR dynamics appear to act as a limiting factor for the penetration limit which cannot be observed when modeling the network using an infinite bus.

3.4.3. Influence of the active power droop gain

As described in Section 3.4.1, the maximum allowable power ratio is around 45% with $x_{eq} = 0.33$ p.u. This value is similar to the 50% that was found in a previous study on the interactions between a similar SM and a VSC in grid-forming mode in a microgrid directly connected to the machine [15]. In order to understand the role of the grid-forming control gains in the stability limit, we perform a parametric study with the $m_{p\omega}$ varying from 1% to 5%. The results are presented in Fig. 13.

It is clear that the droop gain has little influence on the maximum allowable power ratio, because even though it moves the critical eigenvalues in the complex plan, the intersection between the imaginary axis and the rightmost eigenvalues is reached for $P_R \approx 45\%$. On the other hand, when the AVR dynamics are neglected, the system remains stable for all the values of $m_{p\omega}$ we considered.

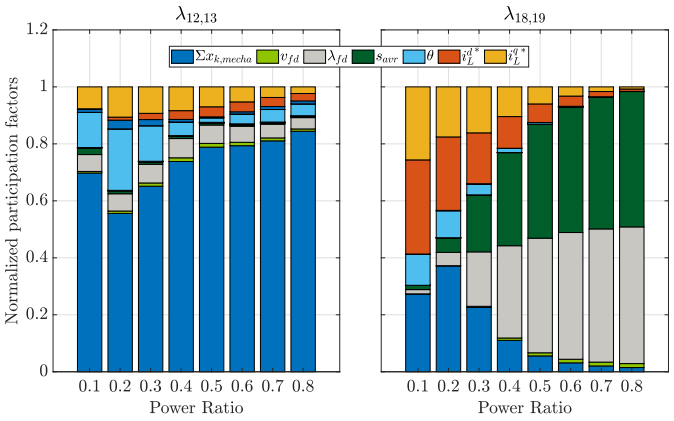

(a) Nominal state-space model

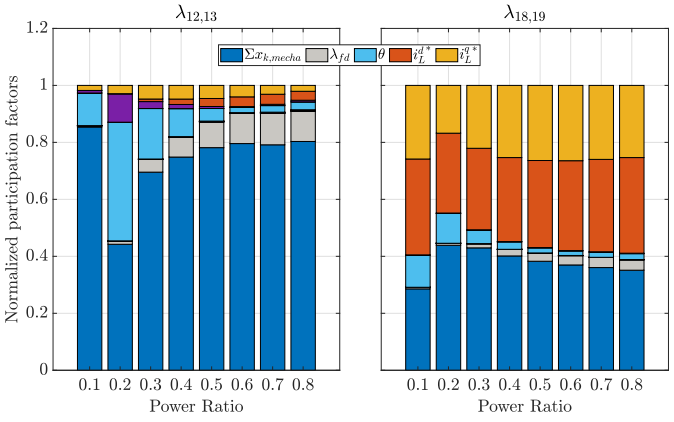

(b) State-space model with no AVR dynamics

Fig. 11. Participation factors of the $\lambda_{12,13}$ and $\lambda_{18,19}$ modes for different values of P_R with the VSC in grid-forming droop mode and $x_{eq} = 0.33$ p.u.

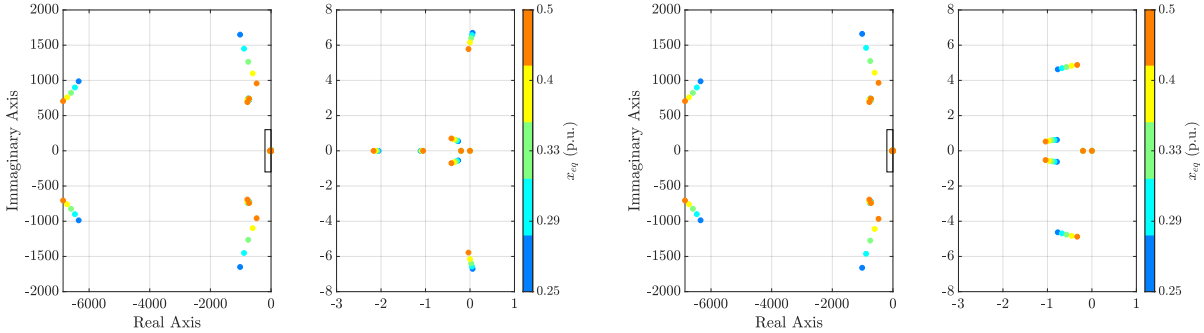

(a) Nominal state-space model

(b) State-space model with no AVR dynamics

Fig. 12. Modal analysis results for different values of x_{eq} with the VSC in grid-forming (droop or VSM) mode and $P_R = 0.45$.

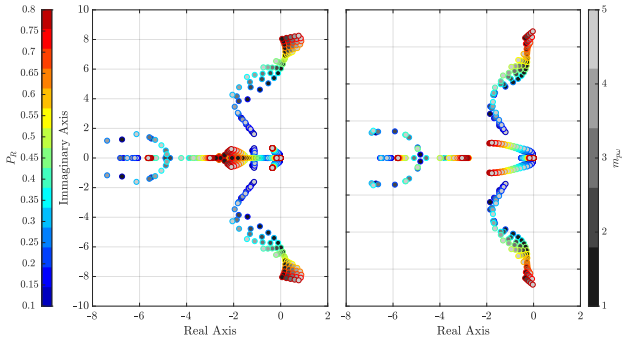

Fig. 13. Modal analysis results for different values of P_R and different droop gains $m_{p\omega}$ with the VSC in grid-forming droop mode and $x_{eq} = 0.33$ p.u. The left-side figure is the nominal state-space model whereas the right-side figure is the state-space model with no AVR dynamics.

This result confirms the conclusions drawn in Sections 3.4.1 and 3.4.2, on the role of the outer power control loop and the AVR of the SM on the critical modes of the system. In addition, we also studied the impacts of the low-pass filter cutoff frequency $\omega_{c,power}$. Since this parameter has no impacts on the eigenvalues, we did not display the results in this paper.

3.5. Comparisons and penetration limit assessment

In order to summarize all the results we obtained for the different VSC control strategies, for different values of the line reactance on the SM and the power ratio, we plot in Fig. 14 the maximum allowable, i.e. stable, power ratio. This gives an indication about the influence of x_{eq} on the system stability. For PLL-based strategies (grid-feeding and grid-supporting), the longer the line, the lower the maximum allowable power ratio. This is an intuitive result since the system stability relies on the PLL algorithm, which is sensitive to the electrical distance to the voltage sources [8]. For grid-forming controls, the impact of the electrical distance is such that the closer the PE is to the SM, the less stable the system becomes.

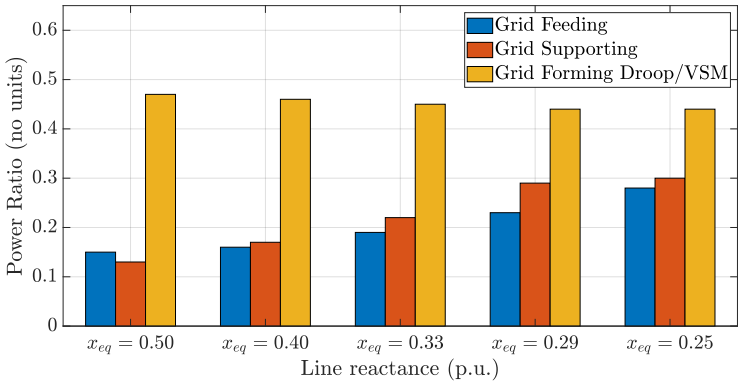

Fig. 14. Maximum allowable power ratio with respect to the line reactance of the system.

To the authors' best knowledge, this result has not been shown in the literature so far and which could drive future research on grid-forming algorithms for improving their penetration limits in power systems. One solution could be introducing a virtual impedance control, as in [14], to electrically "move away" the VSC. However, this control would weaken the PCC voltage stiffness because it would bring farther the voltage source connected to it. Besides, since the electrical distance plays a small role in the stability limit, as described in Fig. 14, it may weaken the grid while bringing no real improvements in terms of small-signal stability.

In addition, for longer lines with $x_{eq} > 0.45$ p.u., the grid-supporting strategy tends to be less stable than the grid-feeding one. As the equivalent voltage source becomes farther, the PLL synchronizes to the grid with difficulty. In fact, the droop actions from (3) is responsible for destabilizing the system.

4. Validation by Simulations

In Sections 4.1 and 4.2, we run time-domain simulations using the nonlinear state-space model developed in Section 2 to verify the modal analysis results given in the previous section. In Section 4.3, we study the stability limit assessments in the case of a multi-machine grid.

4.1. Influence of the power ratio and the electrical distance

Fig. 15 shows the time-domain simulation results on the system when the VSC is controlled in grid-feeding for $P_R = 0.1$ and $P_R = 0.3$ with $x_{eq} = 0.25$ p.u., following a 5% step of active power load. They show that the higher value of P_R results in unacceptable high-frequency voltage oscillations, as predicted by the modal analysis on the stability limits in Fig. 7. Next, we focus on the dependency of the maximum allowable P_R on x_{eq} to quantitatively confirm the results of the modal analysis. We launch a simulation for $P_R = 0.25$ and $x_{eq} = 0.25$ p.u. and introduce a line disturbance such that the line inductance increases up to $x_{eq} = 0.3$ p.u. The evolution of PCC voltage and frequency following this contingency are given in Fig 16. It shows that only the system with the VSC in grid-feeding becomes unstable, which confirms the modal analysis results in Fig. 14. In addition, a large overshoot and a longer settling time can be observed when the VSC is controlled in grid-forming than in grid-supporting. This can result from the self-synchronizing capability of grid-forming techniques. Indeed, with grid-forming, we observe two equivalent oscillators, i.e. the machine and the converter that oscillate together to reach a consensus, whereas in the grid-supporting case, the two oscillators show a leading-following relation: the VSC "follows" the SM oscillations, hence much less interferences. On the other hand, regarding voltage stability, thanks to its explicit inner voltage control loop, the grid-forming ensures better performances than the grid-supporting, which uses the reactive power/voltage droop given in (4).

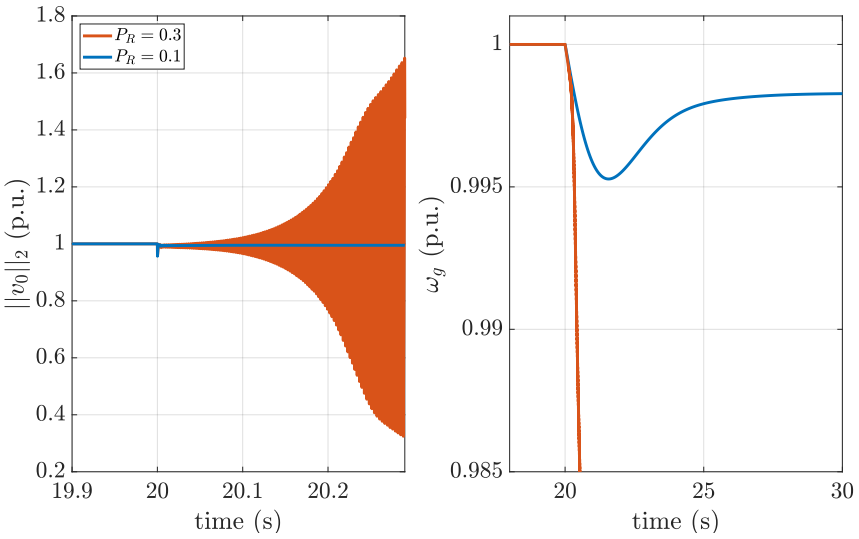

Fig. 15. Evolution of the PCC voltage magnitude and grid frequency following an active power load step at $t = 20$ s when the VSC is controlled in grid-feeding mode for different P_R and $x_{eq} = 0.25$ p.u.

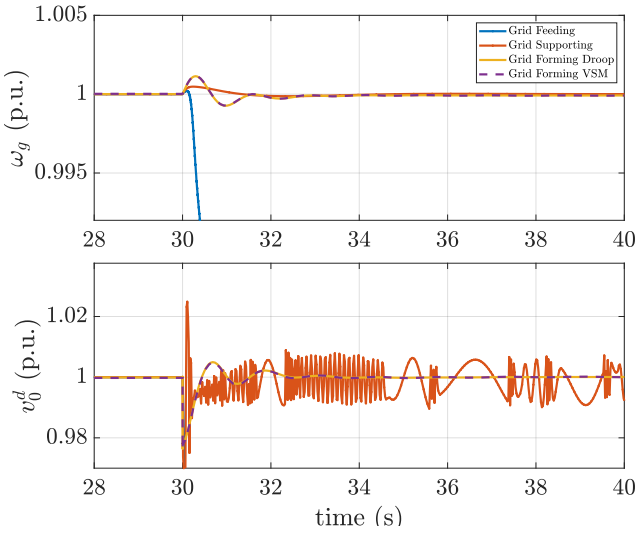

Fig. 16. Evolution of the PCC voltage and grid frequency following a line impedance step at $t = 30$ s with $P_R = 0.25$ and $x_{eq} = 0.25$ p.u.

4.2. Influence of the AVR dynamics

To clarify the relationship between the AVR dynamics and the instability of the system when the VSC is in grid-forming mode, we perform two time-domain simulations for $P_R = 0.5$ and $x_{eq} = 0.33$ p.u., with a 5% step in the load's active power as the disturbance. The simulation results given in Fig. 17 show that the system is unstable when the AVR is taken into account, whereas it remains stable when the AVR dynamics are neglected.

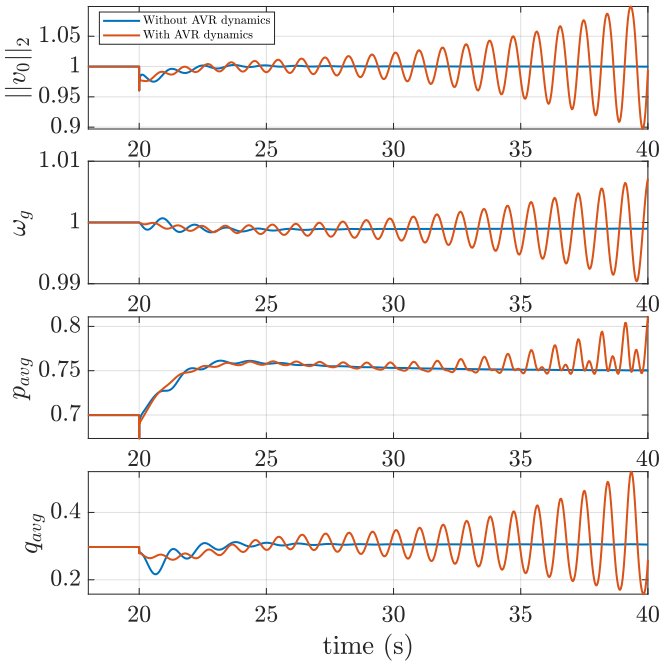

Fig. 17. Evolution of the system state-variables when the VSC is in grid-forming droop mode following an active power load step at $t = 20$ s, with $x_{eq} = 0.33$ p.u and $P_R = 0.5$.

This confirms the modal analysis in Fig. 10. Besides, the frequency of the oscillations is rather slow and may correspond to the undamped low-frequency modes in Fig. 10 in the range of electromechanical dynamics. If such oscillations are caused by the AVR interactions with the grid-forming control, then the use of Power System Stabilizers (PSS) could enhance the compatibility of VSC with the remaining SM. The recent works on penetration limit assessment where the SM is considered with a PSS back this assumption [14].

4.3. Influence of the power system topology

In order to check if the results about the penetration limit assessment given in Fig. 14 can be generalized to more complex systems, we simulate different scenarii with a multi-machine system. For the validation purpose, we choose to consider the much more complicated system shown in Fig. 18, obtained by replacing the SM in Fig. 1 by the 2-area Kundur system defined in [21].

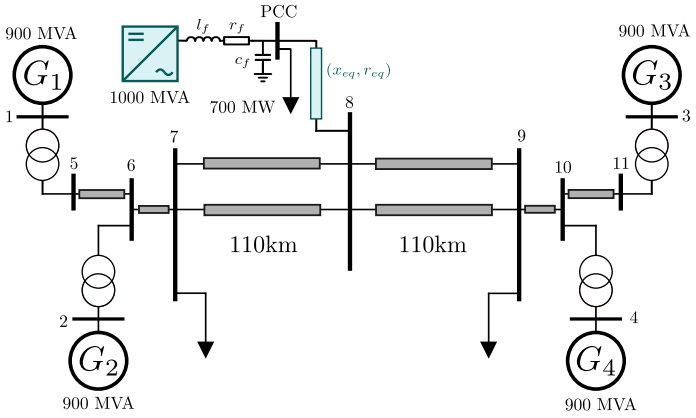

Fig. 18. Modified Kundur's 4-machine, 2-area system, based on [21].

The Kundur's 4-machine system is a 3-phase balanced system of symmetric topology with four 900 MVA SM which was used recently for studying the impacts of power electronics integration in power systems [37]. For the multi-machine system, the VSC model was developed in Modelica language and the Kundur system is based on the iPSL library [38]. The whole system was simulated using Open Modelica software. The initial power flow data and the system bases are given in Appendix 3. Here we have considered a 1000 MVA VSC which corresponds to $P_R = 21.7\%$ based on (1). The VSC control mode and the line reactance of the three cases simulated are summarized in Table 1, in the Kundur system base in order to assess the limits of stability of grid-feeding controlled VSCs when connected to a high impedance grid. The line resistance r_{eq} is calculated accordingly as in Section 2.4.1.

Table 1: Different scenarii using the 4-machines, 2-area system

	VSC control mode	**Line reactance x_{eq}**
Case 1	grid-feeding	0.005 p.u.
Case 2	grid-feeding	0.5 p.u.
Case 3	grid-forming	0.5 p.u.

For the simulation cases, the VSC operates at $p^* = 0.7$ p.u. to match the active power setpoint used so far. The load connected to the PCC is modeled as a constant-current source load to consume 700 MW at the initial voltage. For the grid-feeding cases, the reactive power reference is adjusted to $q^* = -0.065$ p.u. in order to match the absorbed reactive power of Case 3. For the VSC control gains in grid feeding, the control gains are similar to the values from the previous sections. For Case 3 in grid-forming mode, the only differences from Table 2 are the inner voltage controller gains which correspond to a 1000 MVA VSC [39] and $m_{qv} = 0$ in this case study. The VSC in grid-forming mode is operated with a voltage reference

$v_{ref} = v_8^0$ where v_8^0 is the initial value of Bus 8 voltage given in Appendix 3. At $t = 30$s, we introduce a 400 MW load step at Bus 9. The corresponding results for the 3 cases are given in Fig. 19.

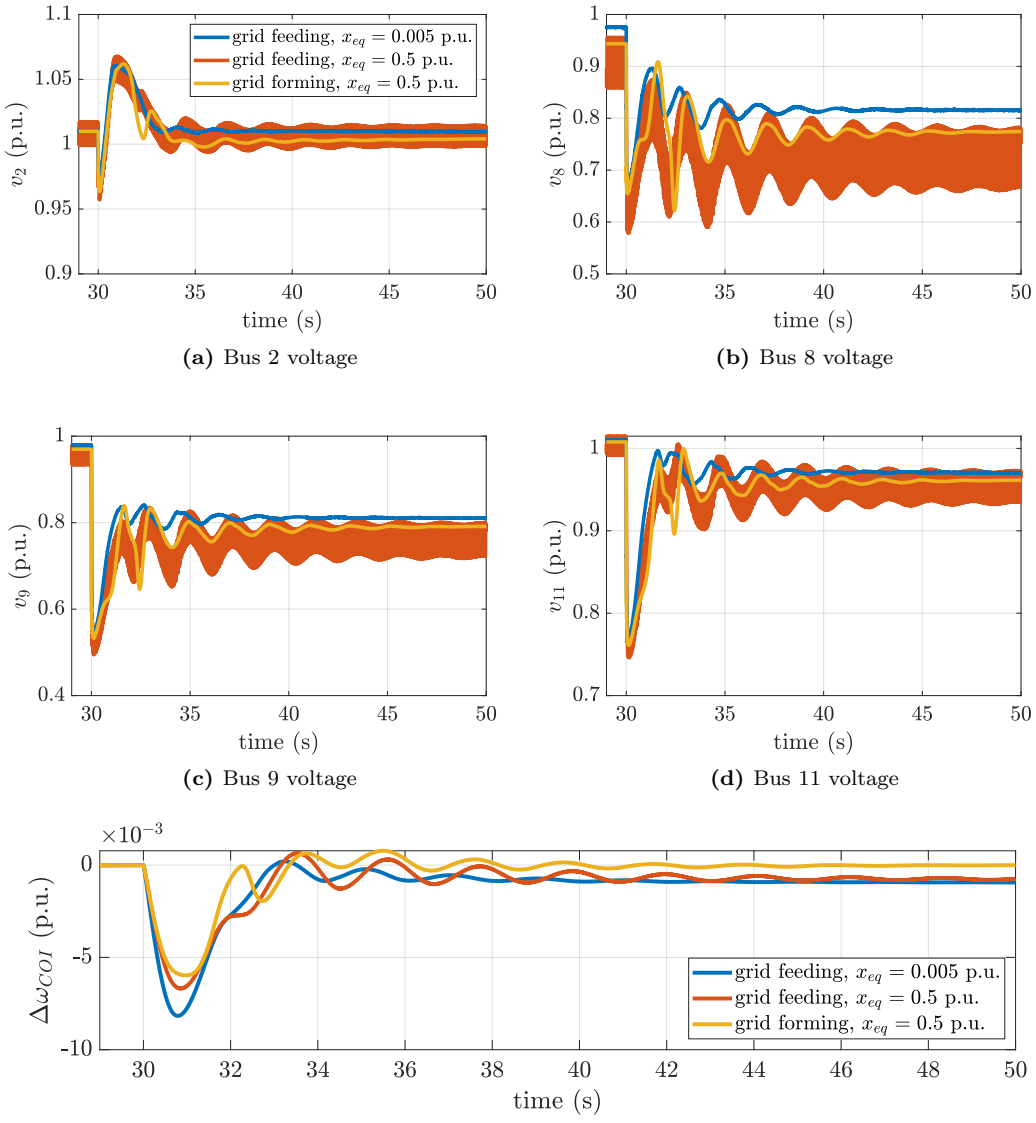

(a) Bus 2 voltage

(b) Bus 8 voltage

(c) Bus 9 voltage

(d) Bus 11 voltage

(e) COI frequency

Fig. 19. Evolution of selected bus voltage magnitudes and COI frequency following an 400 MW active power load step at $t = 30$s at Bus 9 for different VSC control modes and x_{eq}.

v_i corresponds to the i^{th} bus voltage magnitude and $\Delta\omega_{COI} = \omega_{COI} - \omega_{ref}$ is the frequency deviation at the Center of Inertia (COI) which is defined as:

$$\omega_{COI} = \frac{1}{\sum_{i=1}^{4} H_{g_i} S_{g_i}} \cdot \sum_{i=1}^{4} H_{g_i} S_{g_i} \cdot \omega_i \tag{25}$$

where $S_{g_i} = 900$ MVA, H_{g_i} and ω_i are respectively the rated power, the inertia constant and the rotor speed of the i^{th} SM. The slight differences between the voltage setpoints in Figs. 19a to 19d in grid-feeding and

grid-forming modes are due to the changes between the line impedance (x_{eq},r_{eq}).

With grid-feeding, we observe that the bus voltages settle at their steady-state values when $x_{eq} = 0.005$p.u., but show a limit cycle with oscillations at a high frequency when $x_{eq} = 0.5$p.u. Even though the disturbance was introduced at Bus 9 (see Fig. 19c) which has the largest voltage dip, its voltage does not have the largest oscillation magnitude. In particular, the magnitude of voltage oscillations gets larger when the bus is located closer to the VSC (see Bus 8 voltage in Fig. 19b) which suggests they are caused by the VSC operating in grid-feeding mode. In addition, these oscillations become less significant near the SGs (see Bus 2 and Bus 11 voltages in Figs. 19a and 19d). This is in accordance with the claims in Section 3.5 for the case where the P_R is around 20%. In grid-forming, all the bus voltages are brought back to stable operating points when $x_{eq} = 0.5$p.u., which shows the robustness of the control with respect to high-impedance grids.

For the frequency response given in Fig. 19e, we observe a smaller frequency dip for Case 2 than Case 1 but this is due to the voltage-dependent nature of the load at the PCC. However, we still observe low frequency modes in the first two cases, with the frequency of Case 2 less damped than Case 1. In Case 3, the grid frequency deviation exhibits a better response with a smaller frequency dip and a smaller steady-state error, thanks to the frequency support of the grid-forming controlled VSC, while in the grid-feeding cases, the VSC keeps injecting the same power despite the contingency.

5. Conclusions

In this paper, stability issues of AC power network with PE based VSC converters using different control strategies have been highlighted. Rather than using an AC power system solely based on PE, a simplified network with both VSC and SM has been considered in order to show the impact of PE on power system stability. Three VSC control strategies and AVR dynamics of the SM are considered against different values of the power ratio (VSC power rating over SM) and the transmission line length. The following concluding remarks can be pointed out:

- For grid-feeding control, it has been shown that, due to the PLL, stability is lost when the PE penetration ratio becomes too high. This issue can be partially mitigated when using the grid-supporting control, which tolerates a higher PE penetration ratio than the grid-feeding control. In future work, a complementary study could be pursued to take into account the impacts of the control gains, especially the PLL, in the stability limits. Additionally, the influence of the electrical distance between the VSC and SM which has been studied using participation factors has also shown stability issues when the electrical distance is increased. For real power systems, this problem exists but with less impact since the grid buses are reinforced through redundant lines.

- For grid forming controls, i.e. droop and VSM, it has been highlighted that the interactions between the AVR and the VSC control seem to be almost independent of the electrical distance, where stability issues may be caused by the electromechanical resonance with VSC outer-loop controls. In this case the authors would suggest to extend the use of the PSS as a potential solution. This could be done in future work knowing that the interactions between VSCs and SMs may change when considering multiple-bus AC power systems with different types of SMs.

In Section 4.3, time domain simulations were carried out in a multi-machine system. However, the conclusions of this study could be tested in the future with even more realistic power systems where the distribution of the SMs and VSCs corresponds to the energy needs and resources. In future work, stability analysis methods based on attraction regions tools [40, 41] could provide complementary results for understanding the limits of power electronics penetration in AC grids. Moreover, it will be essential to consider the DC-side dynamics of the VSC when studying the overall dynamics of the AC network with the constraints from these new power sources with the role of grid-forming, an aspect that has been up to now rarely addressed in literature.

Aknowledgments

This work is supported by the French Government under the program Investissements d'Avenir (ANEITE-002-01).

APPENDIX

1. SM modeling

In the following, the differential equations are presented in the dq-frame with the q-axis aligned with the rotor.

1.1. Voltage dynamics

The SM is supposed to regulate its voltage v_g at its reference v^* at the connection point. This function is realized by the AVR, which is composed of a lead-lag filter controller and an AC exciter model, as:

$$T_c \cdot \Delta\dot{v} + \Delta v = T_b \cdot \dot{v}_c + v_c \tag{26}$$

$$T_a \cdot \dot{v}_{fd} + v_{fd} = k_a \cdot v_c \tag{27}$$

where $\Delta v = v^* - \|v_g\|_2$, T_b and T_c are the time constants of the lead-lag filter, T_a the exciter time constant, k_a the exciter gain and v_{fd} the field excitation voltage. It is important to note that the dynamics of PSS (Power System Stabilizers) could also have been taken into account, as in [14]. But, since the PSS enhances the system stability and does not reflect the behavior of standard SM with classical AVR schemes, it is not included in our study.

To excite the machine, the AVR uses the field excitation voltage, v_{fd}. The dynamics are modeled as:

$$\dot{\lambda}_{fd} = \omega_{base} \cdot (v_{fd} - r_{fd} \cdot i_{fd}) \tag{28}$$

$$L_{fdfd} \cdot i_{fd} = \lambda_{fd} + L_{afd} \cdot i_g^d \tag{29}$$

where r_{fd} is the rotor winding resistance, i_{fd} the field current, λ_{fd} the field flux, L_{fdfd} and L_{afd} are respectively the self and mutual inductances of the rotor and ω_{base} the system fundamental angular frequency. Using the magnetic couplings between the rotor and the stator, the field current i_{fd} is related to the stator armature current i_g^{dq}, via the stator flux λ^{dq} as:

$$\lambda^d = -L_d \cdot i_g^d + L_{afd} \cdot i_{fd} \tag{30}$$

$$\lambda^q = -L_q \cdot i_g^q \tag{31}$$

The relationship between the stator flux and the terminal voltage v_g^{dq}, as described in [32], with the *copper losses*, modeled with the resistance r_a is given as:

$$v_g^d = -\lambda^q - r_a \cdot i_g^d \tag{32}$$

$$v_g^q = \lambda^d - r_a \cdot i_g^q \tag{33}$$

The electrical power is given by $P_e = \lambda^d \cdot i^q - \lambda^q \cdot i^d$, which neglects the copper losses in the stator.

1.2. Frequency dynamics

The swing equation is related to the dynamics of the rotor speed, and thus of the grid frequency, ω_g. The rotor angle, denoted by δ, corresponds to the integral of the frequency:

$$2 \cdot H \cdot \Delta\dot{\omega}_g + D \cdot \Delta\omega_g = P_m - P_e \tag{34}$$

$$\dot{\delta} = \omega_{base} \cdot (\omega_{ref} + \Delta\omega_g) \tag{35}$$

where ω_{ref} is the grid reference frequency in per unit. The primary frequency control of the machine is realized by a droop controller as:

$$P_{m,gov} = P_m^* - \frac{1}{r_d} \cdot \Delta\omega_g = P_m^* + \Delta P_m \tag{36}$$

where $P_{m,gov}$ is the mechanical power at the governor input. The SM mechanical dynamics, which include the governor and turbine dynamics, are given in Fig. 20, with $P_{m,turb}$ being the mechanical power at the turbine input.

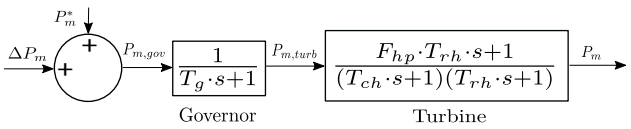

Fig. 20. Transfer function of the governor and turbine model from [3].

2. Numerical values of the test system

Table 2: Numerical values of the system for the simulations.

SM		VSC	
T_c	1 s	$K_{p\omega}$	50 p.u.
T_b	12 s	K_{qv}	0.2 p.u.
T_a	0.04 s	p_{ref}	0.7 p.u.
k_a	0.0745 p.u.	q_{ref}	variable
r_{fd}	0.0006 p.u.	v_{ref}	1 p.u.
L_{afd}	1.66 p.u.	k_{ip}	20 rad/s
L_{fdfd}	1.825 p.u.	$\omega_{c,power}$	31.42 rad/s
L_d	1.81 p.u.	$m_{p\omega}$	2%
L_q	1.76 p.u.	H_c	795.8 ms
r_a	0.003 p.u.	D_c	50 p.u.
H	2.9 s	m_{qv}	0.1%
D	1 p.u.	c_f	0.066 p.u.
r_d	5%	l_f	0.15 p.u.
T_g	0.2 s	r_f	0.005 p.u.
F_{hp}	0.3 p.u.	k_{iv}	2.1008 rad/s
T_{rh}	7 s	k_{pv}	0.0294 p.u.
T_{ch}	0.3 s	k_{ii}	477.5 rad/s
v^*	1 p.u.	k_{pi}	0.6635 p.u.
P_m^*	variable	$k_{i,pll}$	-3603.6 rad/s
ω_{base}	314.16 rad/s	$k_{p,pll}$	-120 p.u.
ω_{ref}	1 p.u.	$\omega_{c,pll}$	200 rad/s
Line		**Load**	
X/R	10	P_{load}	385 MW
U_{base}	24 kVLL	Q_{load}	50 MVAR
S_{base}	550 MVA		

3. Simulation conditions of the Kundur 4-machine, 2-area system

The different values of the initial power flow are given below in the base system where $U_{base} = 400$kV, $S_{base} = 100$MVA and $f_{base} = 60$Hz. The inertia constants are $H_{g_1} = H_{g_2} = 6.5$s and $H_{g_3} = H_{g_4} = 6.175$s. More details about the simulation parameters can be found in [21]. The synchronous generator model is based on a round rotor model from the iPSL library [38]. The AVR is modeled with an excitation system SEXS and coupled with a type II PSS. The governor is a G1 type model.

Table 3: Power Flow data of the Kundur 4-machine, 2-area system

bus #	**1**	**2**	**3**	**4**	**5**	**6**	**7**	**8**	**9**	**10**	**11**
v (p.u.)	1.03	1.01	1.03	1.01	1.007	0.98	0.96	0.95	0.97	0.98	1.009
$\theta(^o)$	20.27	10.51	-6.8	-17.0	13.8	3.71	-4.69	-18.5	-32.15	-23.7	-13.4
P(MW)	700	700	719.1	700	0	0	-967	0	-1767	0	0
Q(MVAR)	185.0	234.6	176.0	202.1	0	0	+84.7	0	+230.2	0	0

References

[1] IPCC, Summary for policymakers, Global Warming of 1.5°C. An IPCC Special Report on the impacts of global warming of 1.5°C above pre-industrial levels and related global greenhouse gas emission pathways, in the context of strengthening the global response to the threat of climate change, sustainable development, and efforts to eradicate poverty (2018).

[2] RTE, Electricity report 2018 (2018).
URL https://bilan-electrique-2018.rte-france.com/?lang=en#
[3] Y. Lin, B. Johnson, V. Gevorgian, V. Purba, S. Dhople, Stability assessment of a system comprising a single machine and inverter with scalable ratings, in: 2017 North American Power Symposium (NAPS), IEEE, Morgantown, WV, 2017, pp. 1–6.
[4] G. S. Pereira, V. Costan, A. Bruyère, X. Guillaud, Impact of synchronous machine dynamics on the stability of a power grid with high penetration of Variable Renewable Energies, in: 15th IET International Conference on AC and DC Power Transmission (ACDC 2019), IET, Coventry, UK, 2019.
[5] G. S. Pereira, V. Costan, A. Bruyère, X. Guillaud, Synchronous machine representations for stability studies of power systems with inverters, in: 2019 IEEE PES Power Tech, 2019.
[6] C. Collados-Rodriguez, M. Cheah-Mane, E. Prieto-Araujo, O. Gomis-Bellmunt, Stability analysis of systems with high VSC penetration: Where is the limit?, IEEE Transactions on Power Delivery (Dec. 2019).
[7] L. R. Castillo, D. A. Roscoe, Experimental stability assessment of converter-dominated electrical grids, in: 16th Wind Integration Workshop, 2017.
[8] J. Z. Zhou, H. Ding, S. Fan, Y. Zhang, A. M. Gole, Impact of Short-Circuit Ratio and Phase-Locked-Loop Parameters on the Small-Signal Behavior of a VSC-HVDC Converter, IEEE Transactions on Power Delivery 29 (5) (2014) 2287–2296.
[9] G. S. Misyris, J. Mermet-Guyennet, S. Chatzivasileiadis, T. Weckesser, Grid Supporting VSCs in Power Systems with Varying Inertia and Short-Circuit Capacity, in: 2019 IEEE PES Power Tech, IEEE, Milano, Italy, 2019.
[10] L. Zhang, L. Harnefors, H.-P. Nee, Power-synchronization control of grid-connected voltage-source converters, IEEE Transactions on Power Systems 25 (2) (2010) 809–820.
[11] Q.-C. Zhong, G. Weiss, Synchronverters: Inverters that mimic synchronous generators, IEEE Transactions on Industrial Electronics 58 (4) (2011) 1259–1267.
[12] F. Milano, F. Dörfler, G. Hug, D. J. Hill, G. Verbic, Foundations and challenges of low-inertia systems (invited paper), in: Power Systems Computation Conference (PSCC), 2018.
[13] U. Markovic, J. Vorwerk, P. Aristidou, G. Hug, Stability Analysis of Converter Control Modes in Low-Inertia Power Systems, in: 2018 IEEE PES Innovative Smart Grid Technologies Conference Europe (ISGT-Europe), IEEE, Sarajevo, Bosnia and Herzegovina, 2018.
[14] U. Markovic, O. Stanojev, E. Vrettos, P. Aristidou, G. Hug, Understanding stability of low-inertia systems, arXiv (2019).
[15] M. M. Siraj Khan, Y. Lin, B. Johnson, M. Sinha, S. Dhople, Stability Assessment of a System Comprising a Single Machine and a Virtual Oscillator Controlled Inverter with Scalable Ratings, in: IECON 2018 - 44th Annual Conference of the IEEE Industrial Electronics Society, IEEE, D.C., DC, USA, 2018, pp. 4057–4062.
[16] S. D'Arco, J. A. Suul, O. B. Fosso, A Virtual Synchronous Machine implementation for distributed control of power converters in SmartGrids, Electric Power Systems Research 122 (2015) 180–197.
[17] U. Markovic, Z. Chu, P. Aristidou, G. Hug-Glanzmann, LQR-based adaptive virtual synchronous machine for power systems with high inverter penetration, IEEE Transactions on Sustainable Energy 10 (3) (2019) 1501–1512.
[18] D. Groß, M. Colombino, J.-S. Brouillon, F. Dörfler, The effect of transmission-line dynamics on grid-forming dispatchable virtual oscillator control, IEEE Transactions on Control of Network Systems 6 (3) (2018) 1148–1160.
[19] C. Arghir, T. Jouini, F. Dörfler, Grid-forming control for power converters based on matching of synchronous machines, Automatica 95 (2018) 273–282.
[20] A. Tayyebi, D. Groß, A. Anta, F. Kupzog, F. Dörfler, Interactions of grid-forming power converters and synchronous machines – a comparative study, arXiv (2019).
[21] P. Kundur, Power System Stability and Control, Electric Power Research Institute Edition, 1, McGraw-Hill, 1994.
[22] J. Rocabert, A. Luna, F. Blaabjerg, P. Rodríguez, Control of power converters in AC microgrids, IEEE Transactions on Power Electronics 27 (11) (2012) 4734–4749.
[23] M.-S. Debry, G. Denis, T. Prevost, F. Xavier, A. Menze, Maximizing the penetration of inverter-based generation on large transmission systems: the MIGRATE project, in: 6th Solar Integration Workshop, 2016.
[24] S. Akkari, Control of a multi-terminal HVDC (MTDC) system and study of the interactions between the MTDC and the AC grids., Phd dissertation, Université Paris Saclay (Oct. 2016).
[25] G. Denis, From grid-following to grid-forming: The new strategy to build 100 % power-electronics interfaced transmission system with enhanced transient behavior, Phd dissertation, Ecole Centrale Lille (Nov. 2017).
[26] M. Molinas, J. Suul, S. D'Arco, P. Rodriguez, Extended stability range of weak grids with voltage source converters through impedance-conditioned grid synchronization, in: 11th IET International Conference on AC and DC Power Transmission, Institution of Engineering and Technology, 2015.
[27] J. Roldan-Perez, A. Gonzalez-Cajigas, A. Rodriguez-Cabero, M. Prodanovic, P. Zumel, Design and analysis of a current-controlled virtual synchronous machine for weak grids, in: 2019 IEEE Applied Power Electronics Conference and Exposition (APEC), IEEE, 2019, pp. 1459–1465.
[28] S. Bacha, I. Munteanu, A. I. Bratcu, Power Electronic Converters Modeling and Control with Case Studies, advanced textbooks in control and signal processing Edition, Springer, 2013.
[29] A. Manoloiu, H. A. Pereira, R. Teodorescu, M. Bongiorno, M. Eremia, S. R. Silva, Comparison of PI and PR current controllers applied on two-level VSC-HVDC transmission system, in: 2015 IEEE Eindhoven PowerTech, IEEE, Eindhoven, Netherlands, 2015, pp. 1–5.
[30] A. A. Nazeri, P. Zacharias, F. M. Ibanez, S. Somkun, Design of Proportional-Resonant Controller with Zero Steady-State Error for a Single-Phase Grid-Connected Voltage Source Inverter with an LCL Output Filter, in: 2019 IEEE Milan PowerTech, IEEE, Milan, Italy, 2019, pp. 1–6.
[31] J. Vorwerk, Small-signal analysis of power systems with low rotational inertia, Semester thesis, ETH Zürich (May 2018).

[32] X.-F. Wang, Y.-H. Song, M. Irving, Modern Power Systems Analysis, Springer, 2008.
[33] N. Grid, Impacts of Declining Short-Circuit Levels, Tech. rep., National Grid ESO (Dec. 2018).
[34] L. Fan, Z. Miao, Wind in Weak Grids: 4 Hz or 30 Hz Oscillations?, IEEE Transactions on Power Systems 33 (5) (2018) 5803–5804.
[35] T. Midtsund, J. A. Suul, T. Undeland, Evaluation of current controller performance and stability for voltage source converters connected to a weak grid, in: The 2nd International Symposium on Power Electronics for Distributed Generation Systems, IEEE, Hefei, China, 2010, pp. 382–388.
[36] R. Ofir, U. Markovic, P. Aristidou, G. Hug, Droop vs. virtual inertia: Comparison from the perspective of converter operation mode, in: 2018 IEEE International Energy Conference (ENERGYCON), IEEE, 2018, pp. 1–6.
[37] G. S. Pereira, V. Costan, A. Bruyére, X. Guillaud, Simplified approach for frequency dynamics assessment of 100% power electronics-based systems, Electric Power Systems Research 188 (Nov. 2020).
[38] L. Vanfretti, T. Rabuzin, M. Baudette, M. Murad, iTesla Power Systems Library (iPSL): A Modelica library for phasor time-domain simulations, SoftwareX 5 (2016) 84–88.
[39] E. Rokrok, T. Qoria, A. Bruyere, B. Francois, X. Guillaud, Classification and dynamic assessment of droop-based grid-forming control schemes: Application in HVDC systems, Electric Power Systems Research 189 (Dec. 2020).
[40] Q. Hu, L. Fu, F. Ma, F. Ji, Large Signal Synchronizing Instability of PLL-Based VSC Connected to Weak AC Grid, IEEE Transactions on Power Systems 34 (4) (2019) 3220–3229.
[41] J. C. Gonzalez-Torres, G. Damm, V. Costan, A. Benchaib, F. Lamnabhi-Lagarrigue, Transient stability of power systems with embedded VSC-HVDC links: stability margins analysis and control, IET Generation, Transmission & Distribution 14 (17) (2020) 3377–3388.